Available online at website: https://journal.bcrec.id/index.php/bcrec

Bulletin of Chemical Reaction Engineering & Catalysis, 21 (3) 2026, xxx-xxx

Original Research Article

Textural Properties and Surface Chemistry of Rice Husk–Derived Biochar and Bio-silica Supports in Ni-Catalyzed Oleic Acid Deoxygenation

Wilson Leonidas Mahene[1], Revocatus Machunda[1], Tom A. Buckman[2], Ali A. Salifu[2,3], Thomas Kivevele[1*]

[1]School of Materials Energy Water and Environmental Sciences (MEWES), Nelson Mandela African Institution of Science and Technology (NM-AIST), Tanzania.
[2]Department of Engineering, Boston College, Massachusetts, United States.
[3]Department of Chemistry, Boston College, Massachusetts, United States.

Received: 22th March 2026; Revised: 9th April 2026; Accepted: 10th April 2026
Available online: 16th April 2026; Published regularly: October 2026

Abstract

Rice husk (RH), an abundant agricultural residue, is a promising precursor for the production of carbon- and silica-based catalyst supports for upgrading lipid feedstocks. Previous studies have shown that RH-derived biochar and biosilica can serve as effective catalyst supports in reactions involving relatively small molecules; however, their application in the deoxygenation of lipid-derived molecules remains largely unexplored. In this study, RH was converted into three distinct supports, desilicated biochar (RH-C), KOH-activated desilicated biochar (RH-AC), and biosilica (RH-SiO_2), which were systematically compared as supports for Ni catalysts in the solvent-free deoxygenation of oleic acid. The supports and catalysts were characterized by BET, TEM, XRD, XPS, and TGA. Ni/RH-AC exhibited the highest surface area (809.8 $m^2.g^{-1}$) but lower mesopore volume than Ni-RH-C, while Ni/RH-SiO_2 showed moderate surface area and minimal microporosity. XPS revealed minimal electronic perturbation of Ni supported on biochar, whereas biosilica induced electron withdrawal. All catalysts predominantly followed the decarboxylation/decarbonylation (deCOx) pathway, although Ni/RH-SiO_2 also exhibited noticeable hydrodeoxygenation (HDO). Ni/RH-C achieved the highest conversion (96%), while Ni/RH-AC and Ni/RH-SiO_2 achieved 76% and 72%, respectively. TGA/DSC analysis showed greater carbonaceous material deposition on Ni/RH-AC than on Ni/RH-C, with Ni/RH-SiO_2 exhibiting the lowest coking. These findings reveal a clear structure-property-performance relationship, revealing that desilicated rice-husk biochar provides higher catalytic activity, whereas biosilica offers greater stability and lower susceptibility to coking. Moreover, excessive chemical activation after desilication appears unnecessary and may even be detrimental.

Keywords: Deoxygenation; fatty acids; desilicated rice husk; biochar; bio-silica; decarboxylation; decarbonylation

How to Cite: Mahene, W. L., Machunda, R. L., Buckman, T. A., Salifu, A. A., Kivevele, T. (2026). Textural Properties and Surface Chemistry of Rice Husk–Derived Biochar and Bio-silica Supports in Ni-Catalyzed Oleic Acid Deoxygenation. *Bulletin of Chemical Reaction Engineering & Catalysis*, 21 (3), xxx-xxx. (DOI: 10.9767/bcrec.20690)

Permalink/DOI: https://doi.org/10.9767/bcrec.20690

1. Introduction

Biomass-derived materials, particularly agricultural residues, are increasingly recognized as sustainable sources for the development of heterogeneous catalysts. Rice husk, an abundant by-product of rice milling, is a particularly attractive precursor for catalyst supports intended for upgrading lipid-based feedstocks. It typically contains 70–80% lignocellulosic material and 20–30% inorganic matter, of which silica (SiO_2) accounts for approximately 85–95%. This distinctive composition allows rice husk to be valorized as a source of both biochar and biosilica for catalytic applications [16]. Such valorization not only mitigates agricultural waste accumulation but also reduces dependence on energy-intensive synthetic support materials and

* Corresponding Authors.
Email: thomas.kivevele@nm-aist.ac.tz (T. Kivevele)

their associated CO_2 emissions [25]. Carbonization and subsequent silica extraction yield porous biochar and biosilica materials [4]. The silica extraction process may employ mild reagents, such as sodium carbonate (Na_2CO_3), thereby enhancing its environmental sustainability.

Several studies have independently investigated rice-husk-derived biochar, particularly in its activated form [8,24], and biosilica [13,27-28] as catalyst supports. Most of these studies have shown that rice husk-derived biochar and biosilica can serve as effective catalyst supports in reactions involving relatively small or simple molecules, such as syngas methanation, bio-oil upgrading, and methane cracking. However, their performance in the deoxygenation of lipid-derived molecules remains insufficiently explored. The few available studies on rice-husk-derived silica and rice-husk-derived biochar as supports for fatty-acid deoxygenation have examined these materials separately rather than within a common comparative framework. For example, Riyandi et al. reported that Ni supported on rice-husk-derived silica was active for oleic acid deoxygenation in ethanol solvent, highlighting the importance of support properties in influencing conversion and liquid-product distribution [30]. Chen *et al.* reported that Ni supported on activated rice-husk-derived biochar outperformed conventional Ni/AC in H_2-free, solvent-free stearic acid deoxygenation [3]. However, a systematic comparison of rice husk-derived biochar and biosilica supports obtained from biochar as a common precursor remains lacking. In addition, the role of chemical activation of pre-desilicated rice husk biochar in controlling porosity, metal dispersion, and deoxygenation performance has yet to be clarified.

Deoxygenation of lipid feedstocks, including triglycerides and free fatty acids, is a key route for producing renewable diesel-range hydrocarbons. These reactions proceed mainly through three pathways: decarboxylation ($deCO_2$), decarbonylation (deCO), and hydrodeoxygenation (HDO), with pathway selectivity depending on catalyst composition, support properties, and reaction conditions [11,18]. Because fatty acids and triglyceride are relatively large, support pore size distribution, pore architecture, and pore accessibility are expected to strongly influence mass transport, active-site utilization, and overall catalytic performance. These considerations make rice husk-derived materials particularly interesting supports for deoxygenation catalysts, since their pore structure can be substantially altered through desilication and subsequent activation.

Nickel-based catalysts have emerged as cost-effective alternatives to noble metals for lipid deoxygenation due to their ability to promote C-O bond cleavage, C-H activation, and hydrogen dissociation [29]. These reactions typically favor decarboxylation and decarbonylation (deCOx) pathways over HDO, which is advantageous due to the lower hydrogen consumption associated with deCOx routes. Although Ni often exhibits lower intrinsic activity than noble metals and may require higher metal loadings or longer reaction times to achieve comparable performance [36] its favorable cost and mechanistic versatility make it attractive for large-scale applications. Nevertheless, its favorable economics and mechanistic versatility make it an attractive candidate for large-scale applications Importantly, several studies have demonstrated that catalyst support properties can substantially influence Ni-catalyzed deoxygenation by altering product distributions, improving kinetics and the relative contributions of deCOx and HDO pathways [9,34]. These characteristics make Ni an ideal platform for systematically probing the effects of rice-husk-derived support materials, desilicated biochar before and after chemical activation and rice-husk-derived biosilica on fatty acid deoxygenation.

In this work, biosilica and biochar supports derived from a common rice husk precursor were comparatively evaluated for Ni-catalyzed deoxygenation, with the biochar examined in both activated and non-activated forms. To the best of our knowledge, a systematic comparison of Ni catalysts supported on rice husk-derived desilicated biochar, activated biochar, and bio-silica for solvent-free oleic acid deoxygenation has not been reported. Oleic acid was selected as a model compound representing triglyceride-derived fatty acids. This design enables the effects of support type and post-desilication activation on pore architecture, Ni surface characteristics, and deoxygenation performance to be systematically examined, thereby providing insight into the structure-performance relationships governing catalytic activity, selectivity, and stability.

2. Materials and Method

2.1. Materials

The chemicals used in this study were commercially available and used without further purification. Anhydrous sodium carbonate 99.0% (Na_2CO_3), nickel(II) chloride hexahydrate 99.9 % ($Ni(NO_3)_2.6H_2O$), hydrochloric acid (HCl), and oleic acid (technical grade, 90%) were purchased from Sigma-Aldrich, while silica was extracted from rice husk carbon. Rice husk carbon was prepared in the laboratory at NM-AIST. Dichloromethane (DCM) was purchased from Merck while N_2 and H_2 gas were of 99.999% purity.

2.2. Preparation of Catalyst

The catalyst preparation procedure involved sequential steps: washing and drying of rice husk, carbonization, demineralization, desilication, chemical activation, metal impregnation, and thermal reduction [37]. Figure 1 presents a summary of the major steps in the catalyst support preparation from rice husk; biochar, activated biochar and silica. Initially, rice husk was thoroughly washed, oven-dried at 105 °C, and placed in a sealed, locally fabricated metallic container designed to limit oxygen ingress. Carbonization was carried out in a muffle furnace without any carrier gas, with the temperature raised to 600 °C at a rate of 10 °C/min and held for 3 hours. The furnace was then allowed to cool naturally to room temperature.

The biochar (20 g) was demineralized by refluxing in 5 wt.% hydrochloric acid (HCl) at 95 °C for 3 h to remove inorganic constituents. The solid was washed with distilled water until the pH of the filtrate reached neutrality and then dried at 105 °C for 12 h prior to desilication. Desilication was conducted by refluxing 15 g of the demineralized biochar in 200 mL of 15 wt.% sodium carbonate (Na_2CO_2) solution for 4 h. Sodium carbonate was selected in preference to sodium hydroxide (NaOH) due to its lower alkalinity, reduced corrosiveness, improved handling safety, and lower environmental burden. The desilicated biochar was recovered by vacuum filtration, thoroughly washed with distilled water until neutral pH, and oven-dried. The resulting sodium silicate solution was acidified dropwise with dilute HCl under continuous stirring until pH of 6 was reached, inducing silica gel formation. The recovered silica was dried at 105 °C for 12 h and subsequently calcined at 500 °C for 2 h in a tubular furnace under a nitrogen atmosphere using a heating rate of 10 °C.min^{-1}.

Activation of the biochar was performed using potassium hydroxide (KOH, 99.5%) as the activating agent. Equal masses of desilicated, dried biochar and ground KOH were mixed in a 1:1 weight ratio. Typically, 8 g of KOH was dissolved in 40 mL of distilled water in a 100 mL beaker, followed by the addition of 8 g of biochar. The mixture was stirred on a magnetic hot plate at 60 °C in a fume hood until it thickened, then placed in an oven set at 70 °C to dry overnight. The dried composite was transferred to a horizontal tube furnace and heated under continuous nitrogen flow (30 mL/min) to prevent oxidation. The temperature was ramped to 700 °C at a rate of 10 °C/min and maintained for 2 hours. After cooling to room temperature, the activated material was thoroughly washed with distilled water under suction filtration until the filtrate reached neutral pH. The material was stored in dried glass bottles for subsequent characterization.

Nickel was incorporated into activated biochar, non-activated biochar, and silica supports by wet impregnation. To achieve a nominal Ni loading of 20 wt.%, the appropriate amount of nickel nitrate hexahydrate ($Ni(NO_3)_2.6H_2O$, 97 %) was dissolved in excess ethanol, and the support material was added. The resulting mixture was stirred for 2 h to ensure homogeneous distribution of the nickel precursor. Ethanol was subsequently removed using a rotary evaporator at 40 °C under reduced pressure, and the impregnated samples

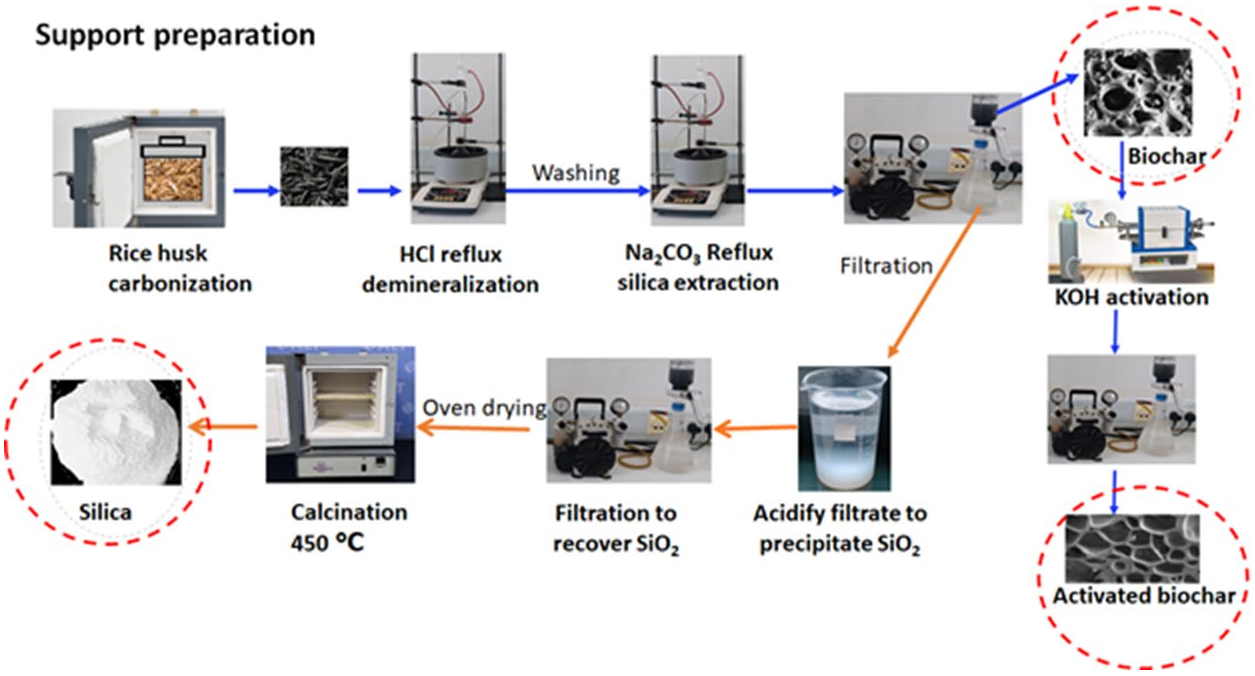

Figure 1. Catalyst support preparation from rice husk; biochar, activated biochar and silica.

were dried under vacuum at 60 °C for 12 h. The Ni-impregnated biochars were then heat-treated at 550 °C under N_2 atmosphere to convert the salt to NiO. Thermal reduction was then performed in a hydrogen atmosphere (99.9% purity) at 550 °C for 4 hours, using a flow rate of 30 mL/min. The temperature was increased to the target temperature at a ramp rate of 5 °C/min. This process yielded metallic nickel catalysts supported on the respective carbon and silica substrates. Figure S1 (Supporting Information) presents the work flow of the Ni impregnation.

2.3. Material Characterizations

Nitrogen adsorption - desorption measurements at -196 °C were conducted using a Micromeritics Gemini 2375 surface area analyzer to determine the specific surface area and pore structure of the activated carbon samples. Prior to analysis, samples were degassed at 200 °C for 12 hours using a Micromeritics FlowPrep 060 to remove physisorbed species. The specific surface area (SSA) was calculated using the Brunauer-Emmett-Teller (BET) method. System integrity was confirmed by leak testing prior to measurement. Total pore volume was determined from the amount of nitrogen adsorbed at a relative pressure of $P/P^0 \approx 0.99$. Pore size distribution and mesopore volume were evaluated using the Barrett-Joyner-Halenda (BJH) method. The average pore diameter was calculated from the relation: $D_P = 4V_T/S_{BET}$. Micropore volume was estimated using the t-plot method with the Harkins-Jura thickness equation. X-ray photoelectron spectroscopy (XPS) was carried out using a ThermoFisher Scientific K-Alpha system. The instrument employs a monochromatic Al Kα radiation source ($h\upsilon$ = 1486.6 eV) and a hemispherical analyzer, operating under ultra-high vacuum (~10^{-9} mbar). Survey and high-resolution spectra were collected to determine the elemental composition and chemical states of surface species. Measurements were carried out with samples mounted on conductive carbon tape. Charging effects were corrected by referencing the C 1s peak corresponding to C-C/C=C bonds to 284.8 eV. High-resolution spectra were deconvoluted after Shirley background subtraction using a Gaussian–Lorentzian mixed line shape (GL(30)). For each core level, peaks associated with the same chemical state were constrained to have equal full width at half maximum (FWHM). The Si 2p spectra were fitted using spin–orbit doublets with a fixed energy separation of 0.6 eV and an area ratio of 2:1. Spectral deconvolution and quantification were performed using Thermo Avantage software. Atomic concentrations were calculated from survey spectra using sensitivity factors supplied by the instrument manufacturer.

Transmission Electron Microscopy (TEM) was employed to examine the internal structure and particle size of the catalysts. For sample preparation, 2 mg of each reduced catalyst was dispersed in 5 mL of ethanol and sonicated for 20 min. A drop of the suspension was deposited onto a carbon-coated copper grid and air-dried for 1 h. TEM images were acquired at an accelerating voltage of 200 kV in bright-field mode. Multiple regions of each sample were imaged to ensure statistical reliability. Particle size distributions were obtained by analyzing more than 100 particles per sample using ImageJ software. Feret's diameter, defined as the longest distance between two parallel lines tangent to the particle perimeter, was used as the particle size metric. Particles were predominantly spherical, and size distributions were generated using a particle area filter of 30-2500 nm² and a circularity threshold ≥ 0.3. Across all samples, metallic Ni nanoparticles were dispersed on the biochar surface, although the degree of dispersion uniformity varied among the catalysts. The average crystallite size (D) was estimated from the Ni(111) reflection using the Scherrer equation (Equation 1).

$$D = K\lambda/(\beta \cos\theta) \quad (1)$$

where K is the shape factor, λ is the X-ray wavelength, β is the instrument-corrected full width at half maximum (FWHM) of the diffraction peak in radians, and θ is the Bragg angle.

2.4. Deoxygenation Procedure

Deoxygenation reactions were carried out in a 50 mL Parr batch reactor (Parr Instrument, model no. 4792-50 mL-T-HC-VGR-DVD-3000-ASME) made of Hastelloy C-276 and rated for operation up to 200 bar at 350 °C. The reactor was equipped with a movable head with thermowell, a 200-bar pressure gauge with gauge adapter and valve, a rupture disk assembly (200-bar disk), a double-valve assembly with dip tube, and a PTFE flat gasket. Reactor temperature was monitored using a K-type thermocouple (Parr, cat. no. D002E4), controlled by a temperature controller (Omega, cat. no. CN7823, 230 VAC), and supplied by a 500 W ceramic band heater (Equilabo, cat. no. FOURMICRO2550K). Figure 2 shows the Parr reactor setup used for the deoxygenation experiments.

Deoxygenation was performed under solvent-free conditions at 340 °C using oleic acid as a model compound for triglyceride-derived fatty acids. In a typical experiment, 15.0 g of oleic acid (90%, Sigma-Aldrich) and 0.75 g of pre-reduced catalyst, previously dried at 105 °C for 6 h, were loaded into the reactor. The system was

purged with N_2 to remove residual air and then pressurized with H_2 (99.999%) to an initial pressure of 30 bar at room temperature. The reaction mixture was heated to 340 °C at a ramp rate of 5 °C.min^{-1} and maintained at this temperature under continuous stirring at 700 rpm for 1, 3, 6, or 8 h, unless otherwise stated. After reaction, the reactor was cooled to room temperature under forced air flow. The reaction mixture was then filtered to separate the solid catalyst from the liquid products. The liquid phase was analyzed by gas chromatography-mass spectrometry (GC-MS, Agilent 7890A) equipped with an HP-5MS column.

Catalytic experiments used for direct comparison of catalyst performance under the standard reaction conditions were performed at 6 h in triplicate, and the results are reported as mean values with the corresponding variability. In contrast, experiments used to track catalytic behavior as a function of reaction time were conducted as single runs and are presented only to illustrate temporal trends, not for statistical comparison. Data are reported as mean ± standard deviation. Differences among the three catalysts were evaluated using one-way analysis of variance (ANOVA), although the results were interpreted cautiously because of the limited sample size. When ANOVA indicated a significant effect, pairwise comparisons were performed using Tukey's honestly significant difference (HSD) post-hoc test. Statistical significance was defined at $p < 0.05$. All analyses were performed using R software. A blank experiment was also performed under the same reaction conditions used for the catalytic tests (340 °C, initial H_2 pressure of 30 bar, 6 h, solvent-free), but in the absence of both catalyst and support.

2.5. Product Analysis

2.5.1. Gas Chromatography–Mass Spectrometry and Flame Ionization Detection (GC-MS/FID) analysis

Quantitative analysis of the reactants and products was performed using a gas chromatography system (Agilent Technologies, Model 7890B) equipped with an autosampler (Model 7963) and a flame ionization detector (FID). Separation was carried out using an HP-5 capillary column (Agilent Technologies; 30 m × 0.320 mm i.d., 0.25 µm film thickness; Cat. No. 19091J-413). Qualitative analysis was conducted using a gas chromatography mass spectrometry system (GC-MS-EI) comprising an Agilent 7890B GC coupled to a 5977A mass spectrometer detector with an electron ionization (EI) source. The system was also equipped with an autosampler (Model 7963). Separation was achieved using an HP-5MS Ultra Inert column (Agilent Technologies; 30 m × 0.250 mm i.d., 0.25 µm film thickness; Cat. No. 19091S-433UI).

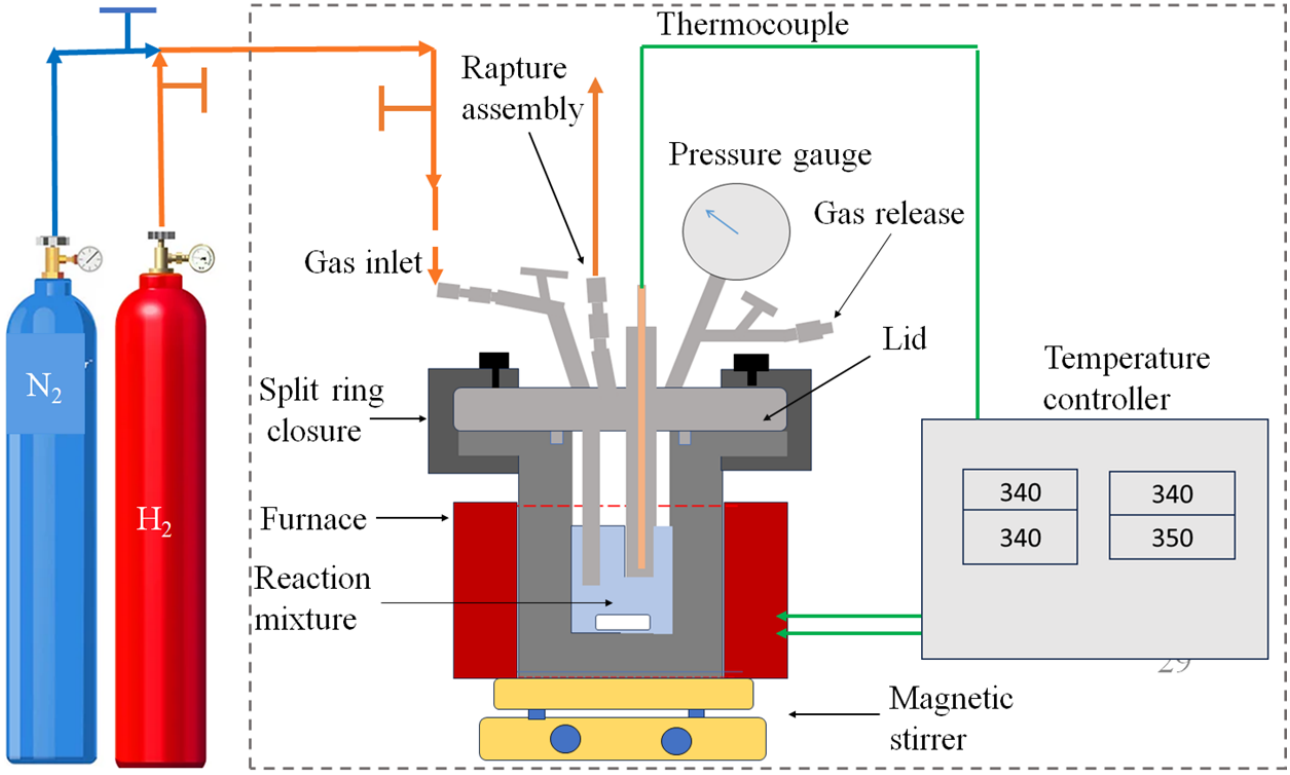

Figure 2. Parr reactor batch set up for deoxygenation reaction. After N_2 purging of the parr reactor and introducing H_2 at 30 bar, the gas cylinders were disconnected. The dotted line represents fume hood.

2.5.2. Sample preparation

Liquid-phase products were diluted in dichloromethane (DCM) at a ratio of 1:25. The diluted sample was filtered under a fume hood using a 0.2 μm syringe filter. After filtration, the sample volume was adjusted back to its original level using DCM to ensure consistency. From the filtered solution, 0.5 mL was mixed with DCM to obtain a final volume of 5 mL. Then, 1 mL of this diluted solution was transferred to a clean vial, and 0.25 mL of a guaiacol internal standard solution was added. DCM was added to bring the total volume to 2 mL. A 1 mL aliquot of this final solution was transferred into a GC vial and injected into either the GC-FID or GC-MS system via autosampler.

2.5.3. Notes on calibration and data analysis

Quantification was based on peak area ratios relative to the internal standard (guaiacol). All measurements were performed in at least three duplicate to ensure reproducibility. Specific GC oven temperature programs, carrier gas flow rates, injector conditions, and detector settings were optimized for the analytes of interest and are available in Table 1.

Product concentrations were quantified using an internal standard method in combination with an effective carbon number (ECN) approach (Equation (2)) [20]. This method assumes that the FID response is approximately proportional to the number of ionizable carbon atoms, with semi-empirical corrections applied for different functional groups in the absence of authentic standards. While this approach enables consistent comparison of product distributions across samples, it provides semi-quantitative estimates, and deviations may arise due to compound-specific response factors, particularly for oxygenated species.

$$Conc_x = \frac{Conc_{std} \times ECN_{std} \times Peak\ A_x}{ECN_x \times Peak\ A_{std}} \quad (2)$$

Where, $Conc_x$ is concentration of an identified compound, ECN_{std} is effective carbon number of internal standard, $Peak\ A_x$ is peak area of an identified compound, ECN_x is effective carbon number of identified compound and $Peak\ A_{std}$ is peak area of an identified compound.

Conversion and Selectivity (carbon-based selectivity) were calculated using Equations (3) and (4), respectively.

$$Conversion\ (\%) = \left(\frac{n_{OA,in} - n_{OA,out}}{n_{OA,in}}\right) \times 100 \quad (3)$$

$$Selectivity, (\%) = \left(\frac{n_i C_i}{\sum n_j\ C_j}\right) \times 100 \quad (4)$$

where n_{OA}, in is the number of moles of oleic acid introduced into the Parr reactor, $n_{OA.out}$ is the number of moles of oleic acid remaining in the reactor at the end of the reaction, n_i is moles of hydrocarbon, C_i is the number of carbon atoms in hydrocarbon and j is all detected hydrocarbon products. Catalytic performances were measured in triplicate.

2.5.4. Metal leaching quantification

Metal leaching was quantified by analyzing the post-reaction liquid phase using ICP-OES after catalyst separation by filtration. The liquid samples were subjected to acid digestion in dilute HNO_3 (3 wt%) to ensure complete dissolution of metal species prior to analysis. This analysis was performed to determine the extent of metal leaching, providing insight into catalyst stability and the potential contribution of homogeneous species. The percentage of metal leaching was determined using the formula Equation (5).

$$\%\ leaching = \frac{n_{metal,liquid}}{n_{metal,cat,0}} \text{x } 100 \quad (5)$$

Where $n_{(metal,\ liquid)}$ is the number of moles of metal in the liquid product and $n_{(metal,\ cat,\ 0)}$ is the initial number of moles of metal in the fresh catalyst.

Table 1. Gas chromatography parameters.

Parameter	Value/degree
Injection volume	1 μL
Septum purge flow	3 mL.min^{-1}
Split flow rate	161.18 mL.min^{-1}
Injection temperature	280 °C
Column temperature	40 °C for 4 min, 2 °C.min^{-1} ramping to 80 °C, 10 min hold at 80 °C, 10 °C.min^{-1} ramping at 300 °C, and 10 min hold at 300 °C
Carrier gas	He at 3.2236 mL.min^{-1} and 13.302 PSI
FID detection temperature	300 °C
FID gases	H_2 at 30 mL.min^{-1}, synthesis air at 400 mL.min^{-1} and N_2 at 25 mL.min^{-1}

3. Results and Discussion

3.1. Characterization of Catalysts

3.1.1. Textural properties

Nitrogen physisorption was used to determine the textural properties of the rice husk-derived supports. All carbon materials exhibited type IV isotherms with H3 hysteresis loops, characteristic of mesoporous materials with slit-shaped pores (Figure 3). Desilication increased the surface area of rice husk carbon from 96 to 617 $m^2.g^{-1}$, likely because removal of silica generated additional pore volume. The pronounced hysteresis loop at $P/P_\circ$ = 0.45-0.9 indicates the presence of mesoporous structures [35]. In addition, the sharp uptake at $P/P_\circ$ = 0.94-1.0 is attributed to capillary condensation in large mesopores and interparticle voids. Desilicated rice husk carbon exhibited a mesopore volume of 0.545 $cm^3.g^{-1}$ (81%), compared with a micropore volume of 0.105 $cm^3.g^{-1}$, confirming its predominantly mesoporous character. As expected, chemical activation of RH-C resulted in a substantial increase in total surface area, accompanied by a marked decrease in mesopore volume. Specifically, the mesopore volume decreased from 0.538 to 0.263 $cm^3.g^{-1}$, whereas the micropore volume increased from 0.112 to 0.457 $cm^3.g^{-1}$. This shift indicates that activation mainly promoted micropore development at the expense of the original mesoporous network, likely altering the silica-templated biogenic pore architecture.

Table 2 summarizes the textural properties of the rice husk-derived supports (biochar, activated biochar, and biosilica) and their corresponding Ni catalysts. Nickel impregnation generally decreased the surface area and total pore volume of all supports, consistent with incorporation of Ni species into the pore network. Despite these decreases, the average pore diameter increased after Ni loading for all catalysts (Ni/RH-C, Ni/RH-AC, and Ni/RH-SiO_2). The total pore volume decreased by approximately 75%, 70%, and 75%

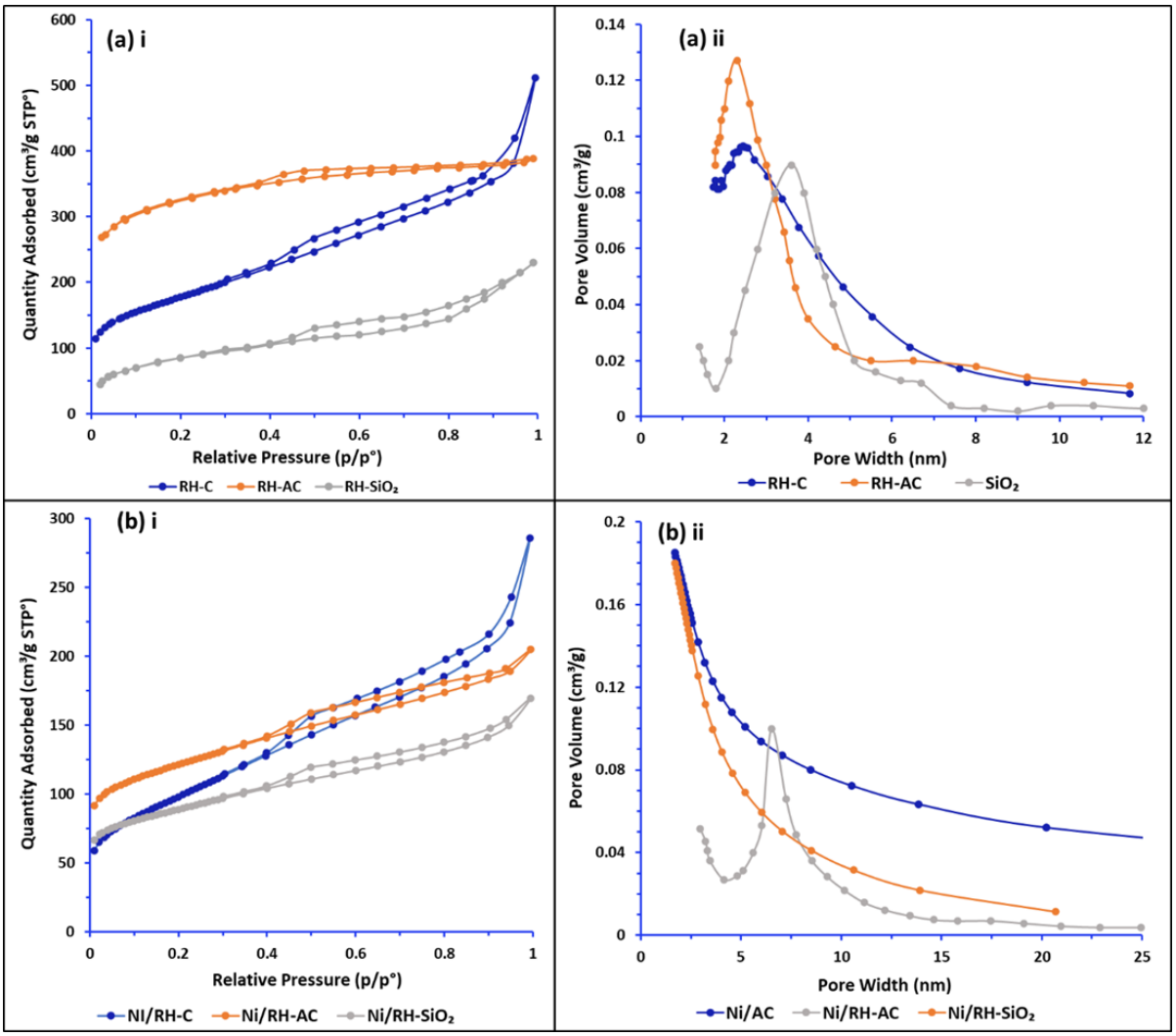

Figure 3. BET isotherms (a) and pore size distribution (b) of rice husk biochar, activated rice husk biochar and rice husk silica, and BET isotherms (c) and pore size distribution (d) Ni supported on rice husk biochar, activated rice husk biochar and rice husk silica.

for Ni/RH-C, Ni/RH-AC, and Ni/RH-SiO_2, respectively. Even after Ni impregnation, Ni/RH-C and Ni/RH-SiO_2 retained relatively high mesopore contributions of 76% and 70%, respectively. By contrast, Ni/RH-AC remained more strongly influenced by microporosity, and the greater loss of micropore volume suggests preferential blocking of the smallest pores following Ni impregnation.

Such pore blocking would reduce nitrogen accessibility during BET analysis, resulting in lower measured surface area and pore volume together with a higher apparent average pore diameter. Although Ni impregnation reduced microporosity and increased the apparent pore size in all samples, this effect was more pronounced for Ni/RH-AC because its pore structure was initially more micropore-dominated. The resulting pore architecture may restrict the accessibility of bulky oleic acid molecules to internal Ni active sites, which could contribute to the lower deoxygenation performance of Ni/RH-AC relative to Ni/RH-C.

3.1.2. TEM analysis of the morphology and dispersion of Ni nanoparticles on RH-C, RH-AC, and RH-SiO_2

The effect of the rice husk-derived biochar- and silica-based supports (RH-C, RH-AC and RH-SiO_2) on the morphology and dispersion of Ni nanoparticles was investigated using Transmission Electron Microscopy (TEM). Figure 4 displays TEM micrographs of the Ni/RH-C, Ni/RH-AC, and Ni/RH-SiO_2 catalysts, alongside their corresponding average particle size and

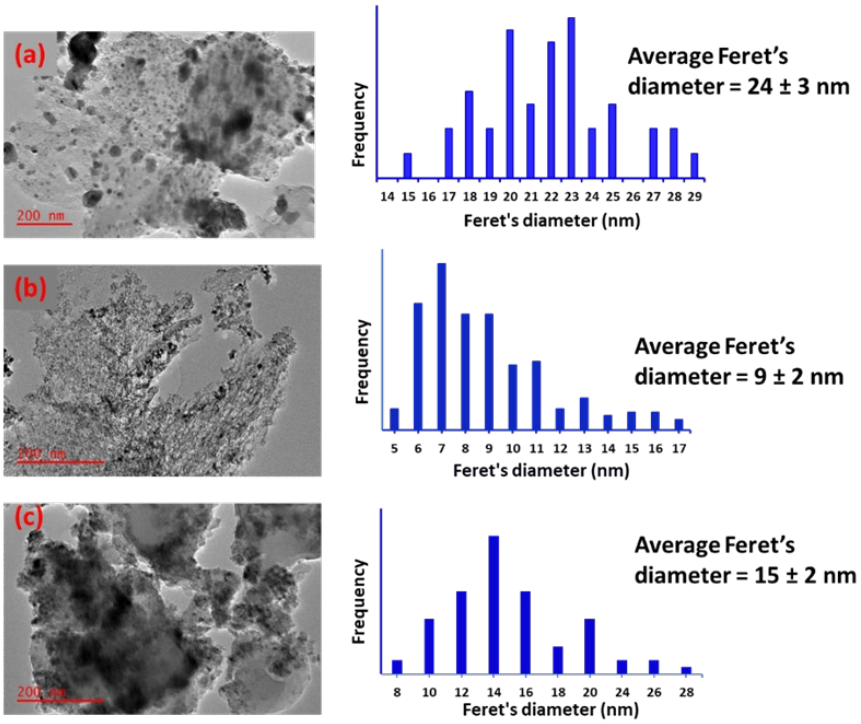

Figure 4. TEM micrographs and particle size distributions of Ni/RH-C (a), Ni/RH-AC (b), and Ni/RH-SiO_2 (c). Particle sizes were measured as Feret's diameter from TEM images of 100 nanoparticles using ImageJ (mean ± SD).

Table 2. Textural properties of rice husk support (biochar, activated biochar and bio-silica) and their respective nickel catalysts.

Support/ Catalyst	SA_{BET}, $m^2.g^{-1}$	Average width nm BJH Desorption APW (4V/A), nm	Pore Volume, cm^3/g	Mesopore volume, cm^3/g	Micropore volume, cm^3/g
RH-C	617	6.175	0.650	0.545	0.105
RH-AC	1030.2	1.868	0.720	0.263	0.457
RH-SiO_2	252	4.100	0.480	0.347	0.133
Ni/RH-C	433.8	8.026	0.285	0.219	0.060
Ni/RH-AC	809.8	5.360	0.212	0.113	0.094
Ni/RH-SiO_2	149.0	5.863	0.360	0.341	0.016

particle size distributions obtained from analysis with *ImageJ* software. The particles are heterogeneous nanoparticles, mostly spherical in shape. The particle size distributions are plotted as frequency versus Feret's diameter. The particle size filter was set to 30-2500 nm² and the circularity threshold to ≥0.3.

From the micrographs, metallic Ni nanoparticles are well-dispersed across the rice husk-derived supports, though with varying degrees of uniformity and aggregation. The average Feret's diameter of the Ni particles follows the order: Ni/RH-C (24 nm) > Ni/RH-SiO_2 (12.5 nm) > Ni/RH-AC (9.5 nm). The smaller particle size observed for Ni/RH-AC compared to Ni/RH-C is indicative of improved dispersion and is attributed to its higher specific surface area and greater density of oxygen-containing functional groups, which serve as anchorage sites for Ni.

In contrast, the significantly larger average particle size observed for Ni/RH-SiO_2 and Ni/RH-C indicates less effective dispersion, likely due to weaker metal-support interactions and reduced anchoring capability relative to the activated carbon-based support. These observations underscore the influence of support properties such as surface area, porosity, and chemical functionality in governing the dispersion and stability of supported metal nanoparticles.

3.1.3. XRD analysis of phase composition and crystallite size

X-ray diffraction (XRD) was used to identify crystalline phases of Ni-containing species and to estimate crystallite size. As shown in Figure 5, the XRD patterns of all samples displayed the characteristic diffraction peaks of metallic Ni at approximately 44.5° (111), 51.8° (200), and 76.4° (220), consistent with crystalline face-centered cubic (FCC) Ni (JCPDS/PDF No. 04-0850) [23]. Crystallite sizes, calculated from the Ni (111) reflection using the Scherrer equation, followed the trend: Ni/RH-AC (3.7 nm) < Ni/RH-SiO_2 (4.7 nm) < Ni/RH-C (7.8 nm). This trend agrees with TEM observations, where particle sizes ranged from ~9-24 nm. The smaller crystallite sizes obtained by XRD compared with the particle sizes observed by TEM suggest that the Ni nanoparticles may be polycrystalline or composed of multiple coherent domains. This observation is consistent with typical reports for Ni-based catalysts, which commonly show polycrystalline particles due to their nucleation and growth behavior during reduction [17]. No peaks corresponding to NiO were detected, suggesting that the reduction treatment effectively produced metallic Ni. The crystallite size values should be regarded as approximate due to inherent limitations of the Scherrer method, particularly in the presence of strain or peak broadening effects [14].

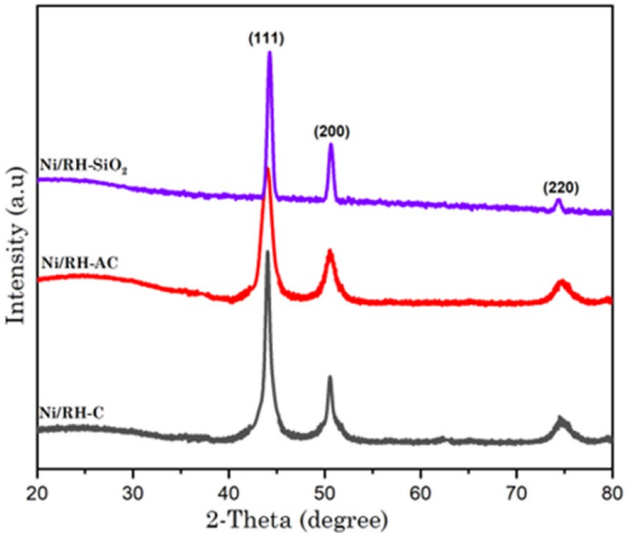

Figure 5. XRD profiles of Ni supported on desilicated rice husk biochar (Ni/RH-C), desilicated and activated rice husk biochar (Ni/RH-AC) and rice husk biosilica (RH-SiO_2).

3.1.4. Surface chemistry of rice husk derived supports and the resulting catalyst

X-ray photoelectron spectroscopy (XPS) was employed to probe the surface chemical evolution of rice husk biochar induced by chemical activation. It was also used to assess the effect of the rice husk-derived supports (RH-biochar, RH-activated biochar, and biosilica) on the electronic structure of Ni. KOH activation can introduce additional oxygen-containing functional groups (OFGs) on the biochar surface, which may influence metal-support interactions and, consequently, catalytic behavior. Quantifying the relative abundance of these groups is therefore important for understanding the performance differences between Ni/RH-AC and Ni/RH-C.

Figure 6 presents the XPS survey spectra and deconvoluted O 1s spectra of desilicated non-activated (RH-C) and activated (RH-AC) biochars. Deconvolution of the O 1s region suggests the presence of three main oxygen species, assigned to O-C=O, C-OH, and C-O-C functionalities, consistent with typical lignocellulosic biochar surfaces [6]. Table 3 summarizes the relative abundance of surface oxygen functional groups in RH-C and RH-AC. Chemical activation induced a marked redistribution of these functionalities. The relative concentration of carboxyl groups increased from 1.1% in RH-C to 2.4% in RH-AC, while hydroxyl groups increased from 6.0% to 7.4%. In contrast, ether-type oxygen decreased from 2.1% to 1.1% after activation. These changes are consistent with partial cleavage of ether linkages and increased surface oxidation, leading to enrichment in more polar oxygen-containing species.

The higher abundance of O-C=O and C-OH groups on RH-AC likely provides a greater density of anchoring sites for Ni precursors, which may contribute to improved Ni dispersion and reduced agglomeration during catalyst preparation. This interpretation is consistent with TEM results showing that Ni/RH-AC exhibits better Ni dispersion than Ni/RH-C. In addition, the higher surface area and pore volume of RH-AC, as indicated by BET analysis, may further facilitate the formation of finely dispersed and accessible Ni species.

The XPS survey spectra of Ni supported on desilicated rice husk biochar and biosilica are shown in Figure S2 (Supporting Information). Figure 7 shows the high-resolution Ni 2p spectra

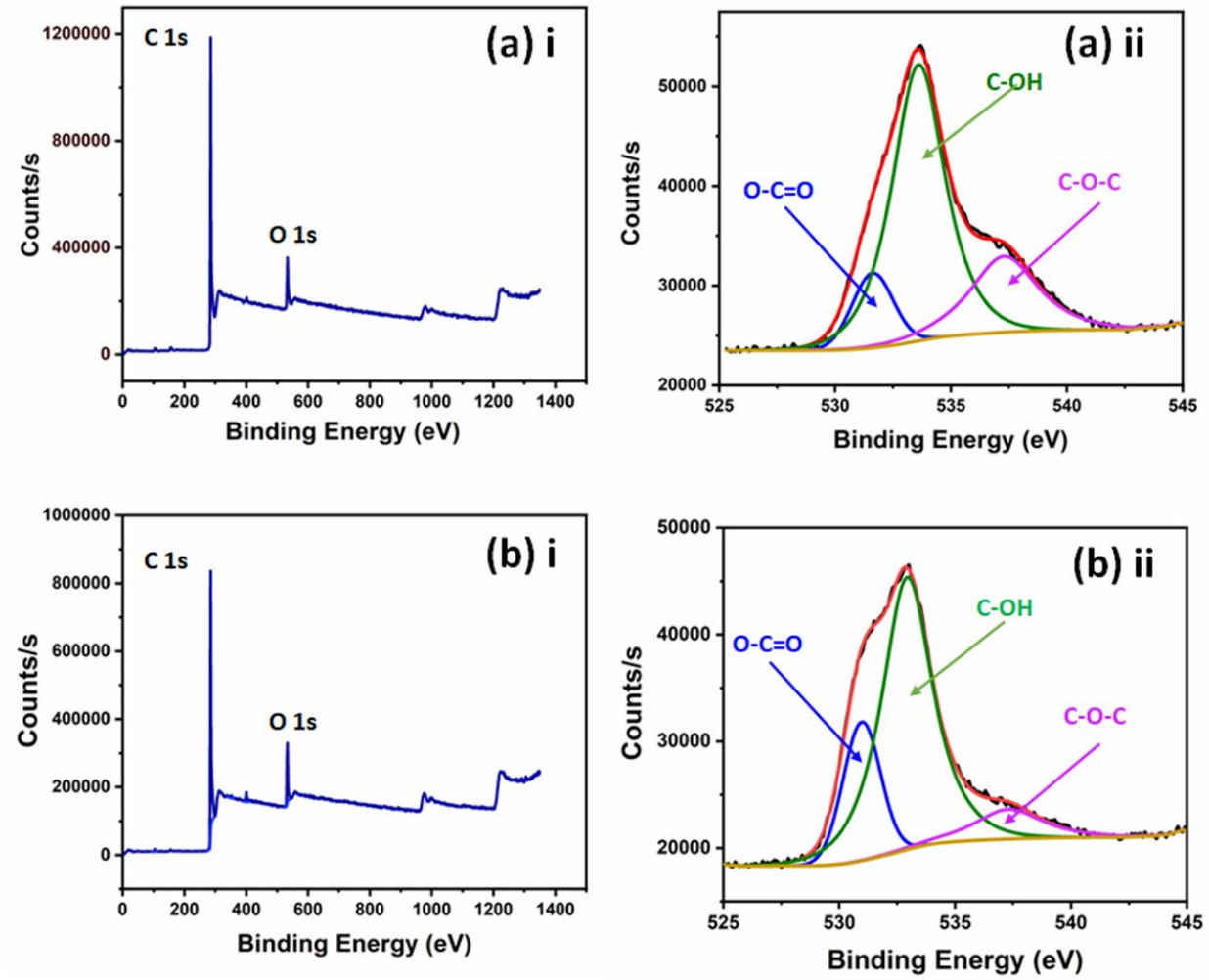

Figure 6. XPS survey and O deconvulated peaks of desilicated rice husk biochar (a) i and (a) ii, and activated rice husk biochar (b) ii and (ii), respectively.

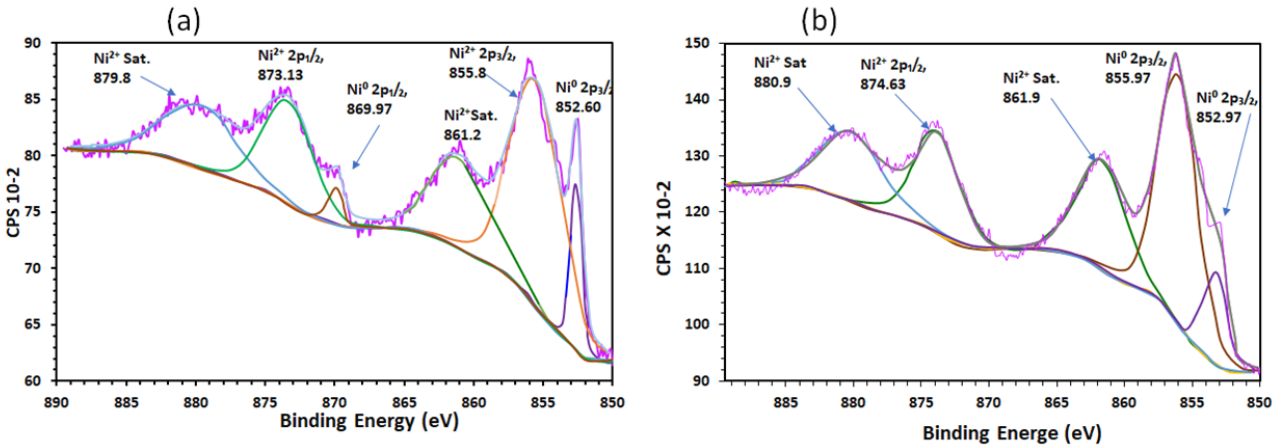

Figure 7. XPS high resolution spectra of Ni/C (a) and Ni/SiO_2 (b). Biosilica (SiO_2) shifts binding energy to higher values indicating electron withdrawal from Ni.

of Ni supported on biochar- and biosilica-based supports, while Table 4 summarizes the Ni 2p binding energies for Ni/RH-C, Ni/RH-AC, and Ni/RH-SiO_2. All catalyst samples exhibited characteristic signals corresponding to both metallic Ni (Ni^0) and oxidized Ni (Ni^{2+}) species. The persistence of Ni^{2+} features despite hydrogen reduction is attributed to partial reoxidation of surface Ni upon exposure to air prior to XPS analysis, a phenomenon commonly reported for Ni-based catalysts [22]. This interpretation is strongly supported by the XRD results, which showed crystalline metallic Ni and no detectable NiO phase, suggesting that the Ni^{2+} species observed by XPS mainly arose from surface reoxidation upon air exposure. The Ni $2p_{3/2}$ binding energies of metallic Ni increased in the order Ni/RH-AC < Ni/RH-C < Ni/RH-SiO_2, with only minor differences between Ni/RH-AC and Ni/RH-C, suggesting a limited electronic perturbation of Ni on the biochar supports and a more electron-deficient Ni environment on biosilica. The higher Ni^0 binding energy observed for Ni/SiO_2 (852.97 eV) is consistent with a surface electron-withdrawing effect of the silica support, which may render the Ni surface slightly more electron-deficient. In contrast, Ni supported on biochar (Ni/RH-C and Ni/RH-AC) exhibits Ni $2p_{3/2}$ and Ni $2p_{1/2}$ binding energies of 852.6 eV and 869.9 eV, respectively, values close to those of bulk metallic Ni. This indicates weak electronic perturbation from the biochar supports. Notably, the Ni^0 $2p_{1/2}$ peak at ~869.9 eV is not observed in Ni/SiO_2. The absence of this feature, which is clearly present in the Ni/C catalysts, suggests differences in the surface reduction state of nickel between the two supports. Both the slight binding-energy shift from bulk metallic Ni and the absence of the Ni^0 $2p_{1/2}$ peak in Ni/SiO_2 point to support-dependent variations in surface reduction behavior and metal-support interactions. While it is plausible that Ni/SiO_2 withdraws electrons from Ni, rendering it partially positive/elecrton deficient, definitive conclusions regarding electronic effects require additional characterization using DRIFTS–CO. These results suggest strong influence of support electronic properties on the Ni electronic structure, with silica inducing stronger metal-support electronic interactions than biochar.

Table 3. Surface oxygen functional groups (OFG) of RH-C and RH-AC samples. Statistical differences among samples were evaluated using one-way ANOVA.

OFG	RH-C	RH-AC	ANOVA p-values
O-C=O	1.10	2.40	0.011
C-OH	6.00	7.35	0.044
C-O-C	2.11	1.09	0.013

3.2. Deoxygenation Performance

The blank experiments resulted in only 1.3 ± 0.3% oleic acid conversion, indicating that non-catalytic conversion under the reaction conditions was negligible relative to the catalyst-assisted runs. The deoxygenation performance of oleic acid over 20 wt.% Ni supported on rice husk-derived biochar (Ni/RH-C), KOH-activated rice husk biochar (Ni/RH-AC), and biosilica (Ni/RH-SiO_2) is summarized in Figure 8a. Representative GC spectra of the corresponding liquid products are provided in Figures S3–S5 (Supporting Information).

For Ni/RH-C and Ni/RH-AC, the major hydrocarbon products were C17 compounds, including 3-heptene, 8-heptadecene, and heptadecane, indicating that the predominant reaction pathway involved decarboxylation / decarbonylation (deCOx) with minimal hydrogenation of the carboxyl group. In contrast, Ni/RH-SiO_2 exhibited a partial shift in product distribution, with C18 hydrocarbons, predominantly octadecane, appearing alongside C17 products, suggesting that hydrodeoxygenation (HDO) contributed to a portion of the deoxygenation. Minor products detected included C8–C18 linear alkanes, such as octane, nonane, decane, tridecane, tetradecane, pentadecane, hexadecane, as well as cyclic compounds, e.g., cyclohexane derivatives (1,4-dimethyloctadecyl and undecylcyclohexane), though these occurred at very low concentrations.

The overall catalytic performance, in terms of oleic acid conversion, followed the order Ni/RH-C > Ni/RH-SiO_2 > Ni/RH-AC. Mean conversions were 96 ± 2% for Ni/RH-C, 76 ± 1% for Ni/RH-SiO_2, and 72 ± 2% for Ni/RH-AC. One-way ANOVA ($F(2,6) \approx 201$, $p < 0.001$), followed by Tukey's HSD post-hoc test, suggested significant differences

Table 4. The XPS Ni 2p binding energy peaks of the reduced Ni/C, Ni/RH-AC and Ni/SiO_2.

Catalyst	Ni^0 $2p_3/_2$	Ni $2p_{3/2}$	Ni $2p_{3/2}$(Satellite)	Ni^0 $2p_3/_2$	Ni $2p_{1/2}$	Ni $2p_{1/2}$(Satellite)
Ni/RH-C	852.6	855.8	861.25	869.97	873.33	879.80
Ni/RH-AC	852.6	855.8	861.26	869.98	873.34	879.70
Ni/SiO_2	852.97	855.97	861.90	-	873.8	880.90

among all three catalysts. However, given the small sample size, the statistical analysis should be regarded as supportive rather than definitive and interpreted with caution. A similar performance trend was observed across 1, 3, 5, and 8 h reaction times, as illustrated in Figure 8b, which shows the variation in C17 hydrocarbon mass, the dominant product, with reaction time. Under the standard reaction conditions, Ni/RH-C also gave the highest selectivity to C10-C17 hydrocarbons, reaching 93% on a molar basis.

The superior performance of Ni/RH-C is likely related to its more favorable textural properties and pore architecture, which may enhance the accessibility of Ni active sites. Compared with Ni/RH-AC, Ni/RH-C exhibits a higher mesopore volume and larger average pore diameter, suggesting a more diffusion-accessible pore network for bulky oleic acid molecules. These mesoporous features may facilitate transport within the catalyst particle and improve the effective utilization of Ni active sites during deoxygenation. By contrast, the lower performance of Ni/RH-AC, despite its higher BET surface area and apparently greater metal dispersion, is likely associated with its predominantly microporous structure. Although mesoporosity is present, the high proportion of microporosity (~45%) may reduce the accessibility of internal Ni sites to oleic acid. dispersion [10]. As a result, the catalytically accessible Ni surface under reaction conditions may be lower than that implied by physical characterization alone, which may contribute to the lower reaction rate.

The structure-activity comparison between activated and non-activated biochar demonstrates that desilicated rice husk biochar does not require chemical activation to achieve a pore structure suitable for the deoxygenation of high molecular weight fatty acids. The additional surface area generated through activation activity is due to microporosity development which did not translate into enhanced catalytic activity. This finding is consistent with previous reports indicating that excessive microporosity restricts access to active sites for large oxygenated molecules such as oleic acid and triglycerides [12,33].

Ni supported on rice husk-derived biosilica (Ni/RH-SiO_2) exhibited higher oleic acid conversion than Ni/RH-AC despite its lower BET surface area. This behavior is likely related to the higher proportion of mesopores in Ni/RH-SiO_2, as indicated by the BET results, which may improve the accessibility of bulky reactant molecules [26]. It may also reflect support-dependent differences in the Ni surface environment that influence catalytic behavior. XPS results showed higher Ni binding energy on the biosilica-supported catalyst than on the biochar-supported catalysts, suggesting that the support influences the surface electronic state of Ni, which may contribute to differences in catalytic behavior. The C17 selectivity for Ni/RH-C, Ni/RH-AC, and Ni/RH-SiO_2 was 85%, 88%, and 81%, respectively, while selectivity toward the C10–C18 hydrocarbon range reached 95%, 94%, and 97%. The high C17 hydrocarbon selectivity observed over Ni/RH-C and Ni/RH-AC suggests that deoxygenation predominantly proceeded via decarboxylation / decarbonylation (deCOx) pathways. In contrast, the partial formation of C18 hydrocarbons over Ni/RH-SiO_2 (12% C18) suggests an increased contribution from hydrodeoxygenation (HDO), highlighting the influence of support type on pathway distribution. Gas-phase product analysis would be required to distinguish decarboxylation from decarbonylation within the overall deCOx pathway; however, such analysis was not carried out in this study. Cracking, cyclization, and aromatization were minimal under the studied conditions, indicating that deoxygenation remained the dominant transformation route.

These observations are consistent with literature reports emphasizing the role of support structure in governing deoxygenation pathways. Riyandi *et al.* [30] reported enhanced HDO selectivity over Ni catalysts in ethanol solvent at

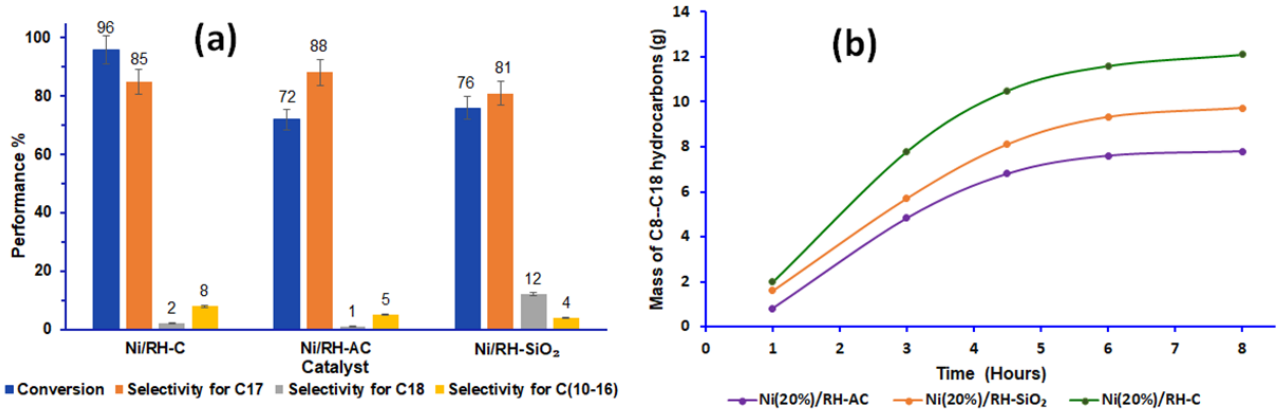

Figure 8. Catalytic performance Ni supported on rice husk derived on biochar (RH-C), activated biochar (RH-AC), and bio-silica (RH-SiO_2) (a), variation of mass of C17 with time (b).

higher catalyst-to-feed ratios; however, their experiments were conducted at lower temperature (285 ˚C), higher hydrogen pressure (40 bar), and shorter reaction times. Despite differences in reaction conditions, both studies demonstrate that support porosity and structure critically influence reactant accessibility and reaction pathway selectivity.

3.3. Reusability and Stability

The reusability of the catalysts Ni/RH-C, Ni/RH-AC, and Ni/RH-SiO_2 was evaluated under identical reaction conditions (340 ˚C, 30 bar H_2) over three consecutive cycles. Between runs, the spent catalysts were recovered by filtration, washed with dichloromethane to remove residual organics, dried, and reused without further regeneration. Thermogravimetric analysis (TGA) coupled with differential scanning calorimetry (DSC) and inductively coupled plasma optical emission spectroscopy (ICP-OES) were used to assess the propensity for carbonaceous deposit formation and Ni leaching, respectively.

The TGA and DSC profiles of all spent catalysts showed additional mass losses and heat-flow features that were not observed in the fresh samples, indicating catalyst modification during reaction. These additional features are consistent with the oxidation of carbonaceous deposits associated with coke precursor formation (Figure 9). Spent Ni/RH-C exhibited a mass loss of

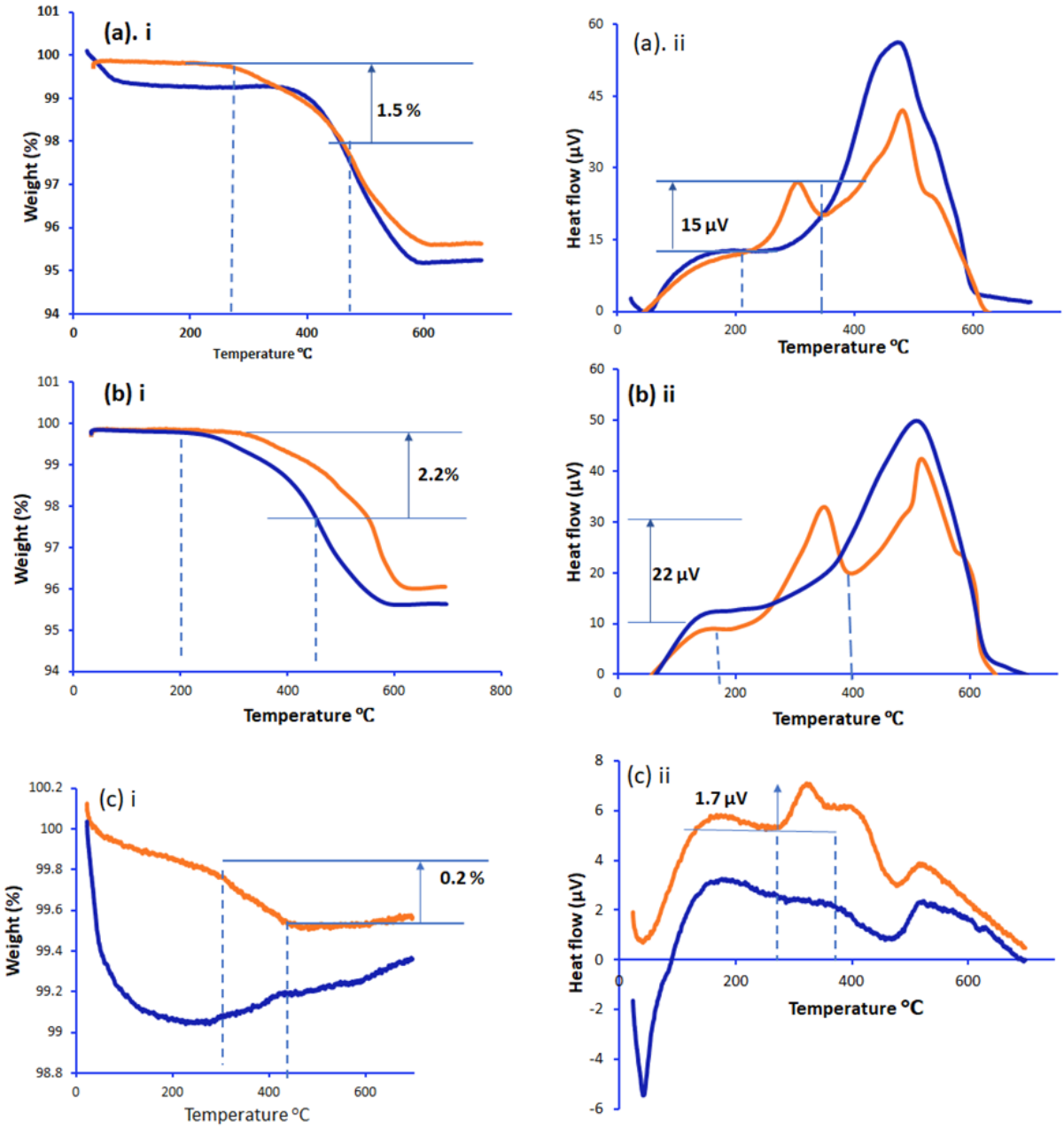

Figure 9. Thermogravimetric Analysis (TGA) and differential Scanning Calorimetry (DSC) of fresh and spent catalysts: (a) Ni/RH-C (i) TGA and (ii) DSC, (b) Ni/RH-AC (i) TGA and (ii) DSC) (C) Ni/ RH-SiO_2 (i) TGA and (ii) DSC. Coking propensity is in the order Ni/RH-AC>Ni/RH-C>Ni/RH-SiO_2.

approximately 1.5 wt% between ~220 and 450 ˚C, accompanied by a pronounced exothermic peak near 320 ˚C (Figure 9a i-ii), consistent with the oxidation of carbonaceous deposits. Spent Ni/RH-AC showed a larger mass loss of ~2.2 wt% over a similar temperature range, with an even more intense exothermic peak near 320 ˚C (Figure 9b i-ii), indicating a greater extent of carbonaceous deposit oxidation. These results suggest that a high degree of microporosity promotes the accumulation of coke precursors and pore blockage, thereby adversely affecting catalyst activity and durability. In contrast, spent Ni/RH-SiO_2 exhibited only ~0.3 wt% mass loss and a relatively weak exothermic feature (Figure 9c i-ii), indicating a substantially lower tendency for carbonaceous deposition and greater thermal stability. The earlier oxidation onset and greater exotherm intensity observed for Ni/RH-AC suggest not only a larger quantity of deposited carbonaceous material, but also a more readily oxidizable fraction, which likely contributed to faster catalyst deactivation. All samples exhibited additional combustion features below approximately 450 °C, suggesting the presence of relatively reactive, less ordered carbonaceous deposits, whereas more refractory and graphitized carbon species generally oxidize at higher temperatures [15,31-32]. Further characterization by Raman spectroscopy and/or microscopy of the spent catalysts, particularly after multiple reaction cycles, would be valuable in future work to better clarify the nature of the deposited carbon species.

ICP-OES analysis revealed cumulative Ni leaching over three cycles in the order Ni/RH-C (3.43 ± 0.04 mg) > Ni/RH-SiO_2 (2.42 ± 0.04 mg) > Ni/RH-AC (1.35 ± 0.04 mg), corresponding to 2.3%, 1.6%, and 0.9% of the initial Ni loading (0.15 g Ni per 0.6 g biochar) (Figure 10), respectively. The catalysts retain activity over three cycles, indicating good short-term stability. The higher Ni leaching observed for Ni/RH-C relative to Ni/RH-SiO_2 is consistent with XPS results, which showed an increase in Ni binding energy when Ni was supported on biosilica, indicative of relatively stronger metal-support electronic interactions. The greater susceptibility of Ni/RH-C to leaching likely contributes to its more pronounced loss of activity upon repeated use. Interestingly, despite experiencing the greatest activity loss, Ni/RH-AC exhibited relatively low Ni leaching. This behavior cannot be attributed to differences in metal-support electronic interactions, as XPS revealed no significant distinction between Ni supported on RH-C and RH-AC. Instead, the reduced leaching from Ni/RH-AC may result from partial confinement of Ni particles within micropores, consistent with the observed decrease in microporosity following Ni impregnation. While such confinement limits Ni loss, coke deposition within micropores can induce pore blockage and diffusion limitations, thereby exacerbating activity loss despite minimal metal leaching.

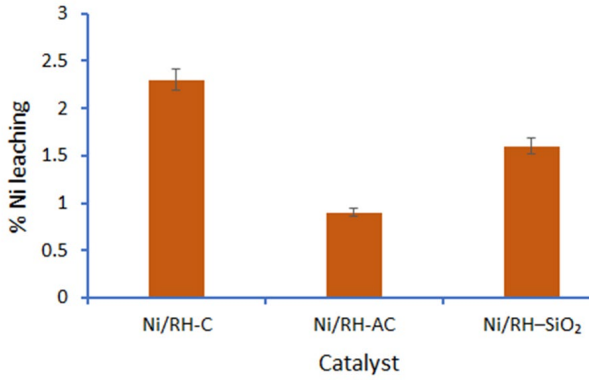

Figure 10. Percent leaching of Ni from Ni/RH-C, Ni/RH-AC and Ni/RH-SiO_2.

The superior reusability of Ni/ RH-SiO_2 can be attributed to the surface chemical properties and pore structure of silica. As a non-reducible, weakly acidic oxide with minimal Brønsted acidity, silica is less likely to promote condensation or polymerization reactions that generate coke precursors during fatty acid deoxygenation, resulting in a lower coking tendency [2,7]. Additionally, both RH-SiO_2 and Ni/RH-SiO_2 exhibited a higher proportion of mesoporosity than Ni/RH-AC, which likely contributes to a reduction in coke formation. This reduced tendency toward coke formation, combined with stronger metal-support interactions as evidenced by XPS, likely accounts for the higher sustained activity observed for Ni/RH-SiO_2 over repeated use [11]. There are relatively few published studies that explicitly compare biosilica and activated carbon derived from the same source as catalyst supports within a single, rigorous performance evaluation. However, studies comparing synthetic silica and activated carbon have shown that differences in pore structure, dispersion, and tortuosity significantly influence coke formation and catalytic performance [21]. These observations are consistent with our findings, wherein activated carbon with a high proportion of microporosity exhibited a greater propensity for coke formation and correspondingly lower catalytic performance.

Figure 11 presents catalyst recyclability of Ni/RH-C, Ni/RH-AC and Ni/ RH-SiO_2 for run/cycle 1-3. After three cycles, Ni/RH-SiO_2 retained 70 ± 2 % of its initial activity, whereas Ni/RH-C and Ni/RH-AC retained only 64 ± 2 % and 50 ± 2 %, respectively (Figure 11). Although Ni/RH-SiO_2 exhibited lower initial activity than Ni/RH-C, its smaller decline over repeated cycles highlights its superior durability. This behavior can be attributed to stronger metal-support interactions between Ni nanoparticles and the SiO_2 matrix,

which effectively anchor the active sites and limit sintering during reuse [5,19]. In contrast, carbon-based supports (RH-C and RH-AC) generally exhibit weaker interactions with Ni, making the metal particles more prone to migration and aggregation, thereby reducing the available active surface area [1]. Moreover, the chemically inert and structurally stable nature of the SiO_2 support enhances resistance to pore collapse, structural degradation, and surface fouling under reaction conditions. The higher initial performance of Ni/RH-C (96%) is attributed to its high mesoporosity (over 80%), which enhances reactant access and activity. However, this catalyst showed greater deactivation than Ni/RH-SiO_2, which is less mesoporous, indicating that mesoporosity alone may not guarantee long-term stability; surface chemistry and metal–support interactions are also critical.

Despite its higher initial specific surface area, RH-AC deactivates more rapidly due to pore filling and blockage by Ni nanoparticles formed during catalyst preparation, as well as by reaction intermediates and carbonaceous deposits during operation. BET analysis indicates that Ni/RH-AC possesses over 50% microporosity, which can exacerbate diffusion limitations and promote pore obstruction. Its decrease in performance over multiple runs compared to Ni/RH-C is also consistent with a higher fouling propensity.

These findings demonstrate that rice husk-derived silica provides a more stable support than biochar, minimizing coke formation and metal leaching, and enabling the repeated use of Ni catalysts for sustainable fatty acid deoxygenation.

4. Conclusion

This study showed that the performance of Ni catalysts in fatty-acid deoxygenation depended on the type of rice husk-derived support and highlighted the potential of rice husk-derived biochar and biosilica as catalyst supports for this reaction. Desilicated biochar (RH-C) gave the highest oleic acid conversion, whereas biosilica (RH-SiO_2) exhibited greater durability and lower carbonaceous material deposition. Although chemical activation of desilicated biochar increased the surface area of RH-AC and led to higher apparent Ni dispersion, this increase mainly resulted from micropore development at the expense of mesoporosity and was accompanied by lower catalytic performance. All catalysts predominantly followed the decarboxylation/decarbonylation (deCOx) pathway, while Ni/RH-SiO_2 showed a small but measurable contribution from hydrodeoxygenation (HDO). The results suggest that rice husk-derived biochar and biosilica provide complementary support properties for Ni-catalyzed deoxygenation of fatty acids, with biochar favoring higher catalytic activity and biosilica enhancing catalyst durability.

Acknowledgment

This research was supported in part by the Junior Faculty Development programmed under the UM6P/EPFL Excellence in Africa Initiative with grant number 9150. Also, the authors gratefully acknowledge The World Academy of Sciences (TWAS) for the support provided under

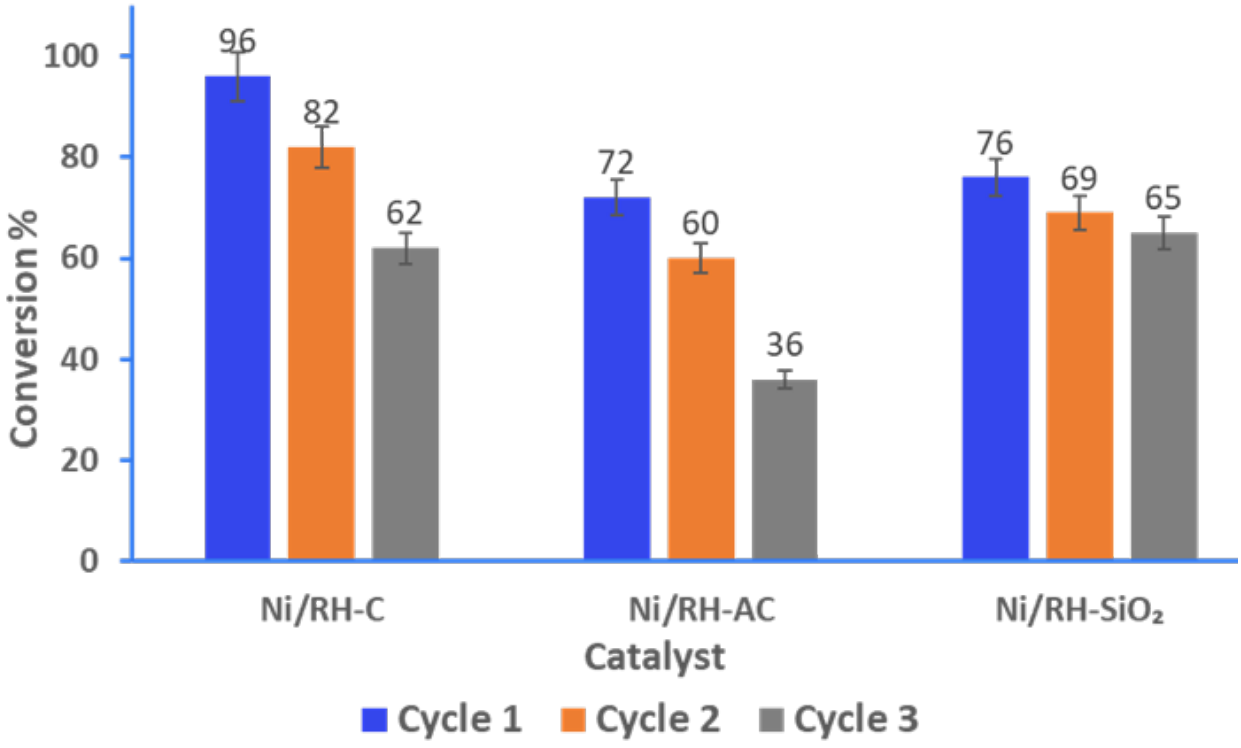

Figure 11. Catalyst recyclability of Ni/RH-C, Ni/RH-AC and Ni/ RH-SiO_2.

the TWAS Research Grant for Individual Scientists (Grant No. 24-006 RG/CHE-OTH/AF/AC_CG – FR, No. 3240339176). Additional support was provided by Boston College through access to the Center for Isotope Geochemistry facilities.

CRedit Author Statement

Author Contributions: Wilson Leonidas Mahene: conceptualization, methodology, investigation, formal analysis, and writing of the original draft. Revocatus Machunda: conceptualization, supervision, validation, and writing-review and editing. Thomas Kivevele: conceptualization, project administration, visualization, and funding acquisition. All authors have read and agreed to the published version of the manuscript.

References

[1] Akamine, Y., Nishino, F., Yamashita, T., Tsushida, M., Awaya, K., Machida, M., Zahan, S.M., Dekel, D.R., Ohyama, J. (2024). The Impact of Metal–Support Interaction on the Structure and Activity of Carbon-Supported Ni Nanoparticle Catalysts for Alkaline Hydrogen Oxidation Reaction. *ACS Applied Materials & Interfaces, 16*(50), 69316-69323. DOI: 10.1021/acsami.4c15120

[2] Bartholomew, C.H. (2001). Mechanisms of catalyst deactivation. *Applied Catalysis A: General, 212*(1-2), 17-60. DOI: 10.1016/S0926-860X(00)00843-7

[3] [3] Chen, B., Cha, X., Dong, X., Bian, J., Huang, J., Li, Q., Huang, X., Zhan, G. (2025). Biochar assembled Ni atom-clusters for hydrogen-free and solvent-free deoxygenation of fatty acids. *AIChE Journal, 71*(7), e18821. DOI: 10.1002/aic.18821Digital

[4] Chen, B., Zhou, Z., Li, Y., Tan, K. B., Wang, Y., Rao, X., Huang, J., Zhang, X., Li, Q., Zhan, G. (2023). Catalytic pyrolysis of fatty acids and oils into liquid biofuels and chemicals over supported Ni catalysts on biomass-derived carbon. *Applied Catalysis B: Environmental, 338*, 123067. DOI: 10.1016/j.apcatb.2023.123067

[5] Chen, C., Wang, W., Ren, Q., Ye, R., Nie, N., Liu, Z., Zhang, L., Xiao, J. (2022). Impact of preparation method on nickel speciation and methane dry reforming performance of Ni/SiO2 catalysts. *Frontiers in Chemistry, 10*, 993691. DOI: 10.3389/fchem.2022.993691

[6] Chen, J., Zhou, J., Zheng, W., Leng, S., Ai, Z., Zhang, W., Yang, Z., Yang, J., Xu, Z., Cao, J. (2024). A complete review on the oxygen-containing functional groups of biochar: Formation mechanisms, detection methods, engineering, and applications. *Science of The Total Environment, 946*, 174081. DOI: 10.1016/j.scitotenv.2024.174081

[7] Choi, D.S., Kim, N.Y., Yoo, E., Kim, J., Joo, J.B. (2024). Enhanced coke resistant Ni/SiO2@ SiO2 core–shell nanostructured catalysts for dry reforming of methane: Effect of metal-support interaction and SiO2 shell. *Chemical Engineering Science, 299*, 120480. DOI: 10.1016/j.ces.2024.120480

[8] Da Pian, G., Braido, R., Alxneit, I., Cruciani, G., Menegazzo, F., Signoretto, M. (2025) Rice Husk Derived Biochar as Support for Ni Based Catalysts in CO2 Methanation: A Study on Biochar Activation. *Applied Catalysis A: General*, 711, 120750. DOI: 10.1016/j.apcata.2025.120750

[9] Dongil, A., Ghampson, I., García, R., Fierro, J., Escalona, N. (2016). Hydrodeoxygenation of guaiacol over Ni/carbon catalysts: effect of the support and Ni loading. *RSC Advances, 6*(4), 2611-2623. DOI: 10.1039/C5RA22540J

[10] Dou, M., Qiao, Y., Hu, X., Miao, H., Zhou, L., Li, X., Hou, X., Wang, Y., Tang, M. (2023). Gradient porous biochar materials with high specific surface area as supports for Pd/C catalysts for efficient maleic acid hydrogenation. *Molecular Catalysis, 545*, 113218. DOI: 10.1016/j.mcat.2023.113218

[11] Fangkoch, S., Boonkum, S., Ratchahat, S., Koo-Amornpattana, W., Eiad-Ua, A., Kiatkittipong, W., . . . Assabumrungrat, S. (2020). Solvent-free hydrodeoxygenation of triglycerides to diesel-like hydrocarbons over Pt-decorated MoO2 catalysts. *ACS omega, 5*(12), 6956-6966. DOI: 10.1021/acsomega.0c00326

[12] Ferreira Young, A., Nothaft Romano, P., Monnerat Araújo Ribeiro de Almeida, J.O., Gomes Aranda, D.A. (2021). Isomerization of oleic acid over acid zeolites: design of experiments and proposal of a novel kinetic mechanism. *Industrial & Engineering Chemistry Research, 60*(39), 14051-14059. DOI: 10.1021/acs.iecr.1c02054

[13] Franco, A., Luque, R., Carrillo-Carrión, C. (2021). Exploiting the potential of biosilica from rice husk as porous support for catalytically active iron oxide nanoparticles. *Nanomaterials, 11*(5), 1259. DOI: 10.3390/nano11051259

[14] Hargreaves, J. (2016). Some considerations related to the use of the Scherrer equation in powder X-ray diffraction as applied to heterogeneous catalysts. *Catalysis, Structure & Reactivity, 2*(1-4), 33-37. DOI: 10.1080/2055074X.2016.1252548

[15] He, L., Liao, G., Li, H., Ren, Q., Hu, S., Han, H., Xu, J., Jiang, L., Su, S., Wang, Y. (2020). Evolution characteristics of different types of coke deposition during catalytic removal of biomass tar. *Journal of the Energy Institute, 93*(6), 2497-2504. DOI: 10.1016/j.joei.2020.08.009

[16] Hossain, S.S., Mathur, L., Roy, P. (2018). Rice husk/rice husk ash as an alternative source of silica in ceramics: A review. *Journal of Asian Ceramic Societies, 6*(4), 299-313. DOI: 10.1080/21870764.2018.1539210.

[17] Islam, M.T., Rahaman, M.A., Ahmed, S., Khatun, M.T., Aman, S., Bayzid, T., Ahmad, A., Al-Amin, M., Alam, M.A. (2025). Effect of Isopropyl Peptization on Surface Particle Growth of Sol-Gel Derived Anatase: X-ray Crystallographic Analysis and Revealed on Transmission Electron Microscopy. *South African Journal of Chemical Engineering, 53*(1), 500-515. DOI: 10.1016/j.sajce.2025.05.007

[18] Jin, W., Pastor-Pérez, L., Villora-Pico, J.J., Pastor-Blas, M.M., Sepúlveda-Escribano, A., Gu, S., Charisiou, N.D., Papageridis, K., Goula, M. A., Reina, T.R. (2019). Catalytic conversion of palm oil to bio-hydrogenated diesel over novel N-doped activated carbon supported Pt nanoparticles. *Energies, 13*(1), 132. DOI: 10.3390/en13010132

[19] Kaviani, M., Rezaei, M., Alavi, S.M., Akbari, E. (2022). High coke resistance Ni-SiO2@ SiO_2 core-shell catalyst for biogas dry reforming: Effects of Ni loading and calcination temperature. *Fuel, 330*, 125609. DOI: 10.1016/j.fuel.2022.125609

[20] Kim, Y.-H., Kim, K.-H., Szulejko, J.E., Bae, M.S., Brown, R.J. (2014). Experimental validation of an effective carbon number-based approach for the gas chromatography–mass spectrometry quantification of 'compounds lacking authentic standards or surrogates'. *Analytica Chimica Acta, 830*, 32-41. DOI: 10.1016/j.aca.2014.04.052

[21] Kohli, K., Prajapati, R., Maity, S.K., Sharma, B.K. (2020). Effect of silica, activated carbon, and alumina supports on NiMo catalysts for residue upgrading. *Energies, 13*(18), 4967. DOI: 10.3390/en13184967).

[22] Kuhaudomlap, S., Mekasuwandumrong, O., Praserthdam, P., Lee, K.M., Jones, C.W., Panpranot, J. (2022). Influence of highly stable Ni2+ species in Ni phyllosilicate catalysts on selective hydrogenation of furfural to furfuryl alcohol. *ACS Omega, 8*(1), 249-261. DOI: 10.1021/acsomega.2c03590

[23] Li, P., Deng, G., Guo, X., Liu, H., Jiang, W., Li, F. (2016). Preparation of nickel and Ni3Sn nanoparticles via extension of conventional citric acid and ethylene diamine tetraacetic acid mediated sol–gel method. *Journal of Alloys and Compounds, 668*, 159-168. DOI: 10.1016/j.jallcom.2016.01.203

[24] Longo, L., Baldassin, D., Di Michele, A., Bittencourt, C., Menegazzo, F., Signoretto, M. (2025). Activation strategies for rice husk biochar: enhancing porosity and performance as a support for Pd catalysts in hydrogenation reactions. *Catalysis Science & Technology, 15*(17), 5101-5115. DOI: 10.1039/D5CY00242G

[25] Nguyen, N.N., Nguyen, A.V., Konarova, M. (2025). Converting rice husk biomass into value-added materials for low-carbon economies: Current progress and prospect toward more sustainable practices. *Journal of Environmental Chemical Engineering*, 115499. DOI: 10.1016/j.jece.2025.115499

[26] Nugraha, R.E., Purnomo, H., Aziz, A., Holilah, H., Bahruji, H., Asikin-Mijan, N.A., Suprapto, S., Taufiq-Yap, Y.H., Jalil, A.A., Hartati, H. (2024). The mechanism of oleic acid deoxygenation to green diesel hydrocarbon using porous aluminosilicate catalysts. *South African Journal of Chemical Engineering, 49*(1), 122-135. DOI: 10.1016/j.sajce.2024.04.009

[27] Peralta, Y.M., Molina, R., Moreno, S. (2024). Chemical and structural properties of silica obtained from rice husk and its potential as a catalytic support. *Journal of Environmental Chemical Engineering, 12*(2), 112370. DOI: 10.1016/j.jece.2024.112370

[28] Peralta, Y.M., Molina, R., Moreno, S. (2024). Rice HUSK silica: A review from conventional uses to new catalysts for advanced oxidation processes. *Journal of Environmental Management, 370*, 122735. DOI: 10.1016/j.jenvman.2024.122735

[29] Prangklang, D., Tumnantong, D., Yoosuk, B., Ngamcharussrivichai, C., Prasassarakich, P. (2023). Selective deoxygenation of waste cooking oil to diesel-like hydrocarbons using supported and unsupported NiMoS2 catalysts. *ACS Omega, 8*(43), 40921-40933. DOI: 10.1021/acsomega.3c06188

[30] Riyandi, R., Rinaldi, N., Yunarti, R.T., Dwiatmoko, A.A., Simanjuntak, F.S.H. (2024). Effect of various silica-supported nickel catalyst on the production of bio-hydrocarbons from oleic acid. *International Journal of Renewable Energy Development, 13*(4), 601-607. DOI: 10.61435/ijred.2024.60054

[31] Sofi, M.H.M., Hamid, M.Y.S., Jalil, A.A., Abdullah, T.A.T., Mohamud, M.Y., Bahari, M., Hassan, N.S., Vo, D.V.N. (2025). Enhanced stability and coke resistance in methanol to olefins reaction using fibrous silica-wrapped silicoaluminophosphate zeolite. *Environmental Chemistry Letters, 23*(6), 1467-1472. DOI: 10.1007/s10311-025-01845-4,

[32] Sun, J., Yamaguchi, D., Tang, L., Chiang, K. (2025). Unravelling carbon formation behaviour and long-term stability of dry reforming of methane over Ru-doped ceria-zirconia catalyst. *Journal of CO2 Utilization, 97*, 103131. DOI: 10.1016/j.jcou.2025.103131

[33] Sun, K., Lu, J., Ma, L., Han, Y., Fu, Z., Ding, J. (2015). A comparative study on the catalytic performance of different types of zeolites for biodiesel production. *Fuel, 158*, 848-854. DOI: 10.1016/j.fuel.2015.06.048

[34] Umenweke, G.C., Pace, R., Récalt, T., Heintz, O., Caboche, G., Santillan-Jimenez, E. (2025). Support Effects on Fe-or Cu-Promoted Ni Catalysts Used in the Catalytic Deoxygenation of Tristearin to Fuel-like Hydrocarbons. *Catalysts, 15*(5), 501. DOI: 10.3390/catal15050501

[35] Wan, Y., Hu, Y., Zhou, W. (2022). Catalytic mechanism of nitrogen-doped biochar under different pyrolysis temperatures: The crucial roles of nitrogen incorporation and carbon configuration. *Science of The Total Environment, 816*, 151502. DOI: 10.1016/j.scitotenv.2021.151502

[36] Wu, J., Shi, J., Fu, J., Leidl, J.A., Hou, Z., Lu, X. (2016). Catalytic decarboxylation of fatty acids to aviation fuels over nickel supported on activated carbon. *Scientific Reports, 6*(1), 27820. DOI: 10.1038/srep27820

[37] Zhang, Z., He, W., Zheng, J., Wang, G., Ji, J. (2016). Rice husk ash-derived silica nanofluids: synthesis and stability study. *Nanoscale Research Letters, 11*(1), 502. DOI: 10.1186/s11671-016-1726-9